Petroleum Science 23 (2026) 3320–3333

Contents lists available at ScienceDirect

Petroleum Science

journal homepage: www.keaipublishing.com/en/journals/petroleum-science

Original Paper

Pressure-regulated pore structure evolution and dielectric performance enhancement in MgO/epoxy composite systems

Hong-Liang Zhang [a,*], Shu-Xuan Li [a], Si-Liang Du [a], Ying-Xin Zhang [a], Su-Fang Li [a], Hai Jin [a], Yao-Min Liu [b], Tao Wu [b]

[a] *School of Automation and Electrical Engineering, Lanzhou University of Technology, Lanzhou, 7300050, Gansu, China*
[b] *China National Petroleum Corporation Baoji Petroleum Pipe Industry Co., Ltd., Baoji, 721008, Shaanxi, China*

ARTICLE INFO

Article history:
Received 22 July 2025
Received in revised form
11 February 2026
Accepted 27 February 2026
Available online 3 March 2026

Edited by Jia-Jia Fei

Keywords:
Downhole electric heater
End-sealing
MgO/epoxy composites
Electric field mitigation
Breakdown reliability

ABSTRACT

With the surging demand for unconventional oil and gas extraction, the insulation performance of downhole high-power electric heaters has become a critical bottleneck limiting long-term stable operation. The MgO/epoxy system is an ideal option for end-sealing materials, yet the mechanism underlying the formation of cascading discharge paths and the insulation failure threshold under extreme conditions, such as in enclosed environments and micrometer-scale gap arrays (<100 μm), remains unclear. Therefore, this study prepared MgO matrices at five pressure levels (30–70 MPa), quantitatively characterized the pore size distribution via FE-SEM, injected epoxy resin to fill pores under vacuum assistance, and established a 2D one-way coupled phase-field-electrostatic model based on the Carreau-Yasuda constitutive law. Results indicate that pressing pressure regulates pore geometric features through sliding, particle rearrangement, and interparticle mechanical interlocking, thereby influencing the infiltration paths and depth of epoxy resin. Additionally, through dielectric constant gradient effects and geometric smoothing, microscopic electric field distortion is effectively mitigated, significantly enhancing the dielectric breakdown characteristics of the composite system, providing a quantitative basis for optimizing the design of end-sealing materials for high-power electric heaters.

1. Introduction

With the strategic shift in global energy structures, the efficient exploitation of unconventional hydrocarbon resources—particularly oil shale and tar-rich coal—has emerged as a pivotal guarantee for national energy security (Kang et al., 2020; Xia et al., 2019). Among various exploitation techniques, the in-situ conversion process (ICP) using downhole high-power electric heaters is widely recognized as the most promising approach due to its precise temperature control and higher thermal efficiency than traditional fluid-injection methods (Chen et al., 2022; Melnikov et al., 1970). As the "heart" of the ICP system, the operational stability of these heaters under extreme downhole environments directly determines the economic viability and safety of the extraction project (Yu et al., 2025). However, with surging demand for higher power density and deeper deployment, the insulation performance of the heater's end-sealing materials has become a critical bottleneck, limiting long-term, stable operation. Consequently, these end-sealing materials should not only maintain excellent mechanical sealing under extreme conditions (Chen et al., 2022) and at pressures exceeding 100 atm (Shui et al., 2023) but also exhibit superior electrical insulation and thermal stability (Yatimi et al., 2024; Xia et al., 2019).

The MgO/epoxy composite system is an ideal option for end-sealing applications due to MgO's high thermal conductivity and epoxy resin's excellent filling capability (Ge et al., 2020; Cha et al., 2024). However, residual micropores and interfacial defects in MgO matrices can form field-enhanced regions under electric fields, significantly reducing the dielectric breakdown strength and triggering localized breakdown failures (Rodríguez-Serna et al., 2020). Moreover, uneven epoxy infiltration or air entrapment creates weak points in the electric field, further increasing the risk of breakdown (Kurimoto et al., 2019).

* Corresponding author.
E-mail addresses: zhanghl312@lut.edu.cn, 55833005@qq.com (H.-L. Zhang).
Peer review under the responsibility of China University of Petroleum (Beijing).

https://doi.org/10.1016/j.petsci.2026.02.024
1995-8226/

Most current studies treat infiltration processes and electric field distribution as independent aspects in epoxy/porous media systems. For instance, Liu et al. (2015) reported the coupling between dielectric response and pore structure in porous media, proposing a micro-capacitor viewpoint that links electrical response to saturation. Hassan et al. (2021) optimized high-pressure resin-impregnation parameters using silicon micromodels and confocal laser scanning microscopy (CLSM) and micro-CT to assess the effects of resin shrinkage and gas entrapment on impregnation quality. Agrawal and Satapathy (2014) investigated the thermal and dielectric properties of ceramic particle-filled epoxy composites and explored the influence of filler volume fraction. Zhang et al. (2015) used a 3-D pore-network model to analyze electrokinetic coupling of fluid flow at the pore scale, providing numerical methods for electric–flow coupling. Cao et al. (2023) constructed ultrathin Al_2O_3 parallel-plate microcapacitors and analyzed dielectric properties in Al-epoxy composites using finite element simulations. Akin and Arikan (2022) simulated localized electric fields for different electrode–material combinations, revealing how electric-field distortion at interfacial defects affects breakdown mechanisms. Karlis (2021) used MATLAB/Simulink to build a capacitive model of partial discharge in epoxy resin and experimentally studied factors such as humidity. Aliyu et al. (2024) employed COMSOL-MATLAB co-simulation to analyze partial discharge behavior under varying frequencies. None of these studies coupled one-way infiltration processes with electric field distribution.

To address this gap, this study developed a 2D multiphysics model of Cahn-Hilliard phase-field coupled with Brinkman-Darcy flow and Carreau-Yasuda rheology, based on pore geometries extracted from real SEM images using Fiji. The model was implemented in COMSOL Multiphysics for joint simulation of phase field infiltration and electrostatic fields. Experiments involving vacuum-assisted epoxy injection (50 °C/40 kPa) and HDGT 10 kV withstand voltage tests were conducted on MgO matrices compacted at five densities (30–70 MPa). This integrated approach aims to elucidate how the porous structure of MgO influences the evolution of epoxy resin penetration paths and local electric-field distortion, and how this infiltration behavior affects the dielectric breakdown performance of the composite system.

2. Experiment and characterization methods

2.1. Dry-pressing preparation and microstructural characterization of MgO pellets

MgO pellets were prepared through dry pressing under humidity <30% (Castillo et al., 2019). First, 20.4 g of high-purity MgO powder (≥99.9%, particle size 1–5 μm) was weighed using a precision analytical balance (JJ224BC, G&G). Subsequently, 0.61 g of deionized water (3 wt% moisture content) was added via a microsyringe. The mixture was stirred with a glass rod until a non-adhesive wet-powder state was achieved. The mixture was then loaded into a uniaxial stainless-steel mold (inner diameter 30.05 ± 0.2 mm) and pre-pressed at 10 MPa for 1 min to evacuate air. During the main pressing stage, a hydraulic press (MCFS-80) applied five pressure levels (30, 40, 50, 60, and 70 MPa) at a rate of 5 MPa/s, with each pressure held for 6 min and repeated three times. After depressurization and coding, pellets were dried in a forced-air oven (8401-0, Shangcheng) using a stepwise protocol: 80 °C (10 min) → 120 °C (5 °C/min, 10 min) → 300 °C (5 °C/min, 30 min). Finally, pellets were equilibrated in a desiccator for 4 h (Fig. 3). Upon cooling to room temperature, pellet radius r and thickness h were measured using a digital micrometer, apparent density was calculated according to $\rho = \frac{m}{\pi r^2 h}$, porosity was calculated as $P = \left(1 - \frac{\rho_m}{\rho_t}\right) \times 100\%$, where the measured density ρ_m was determined from the specimen mass (m) and thickness (h), and the theoretical density was taken as $\rho_t = 3.58\ \text{g/cm}^3$ (Ha et al., 2025). To investigate the effect of pressing pressure on pore morphology, pellets prepared at 30–70 MPa were characterized by field-emission scanning electron microscopy (FE-SEM, SU8020, Hitachi). Cylindrical specimens (⌀5 mm) sectioned along the centerline were polished with diamond sandpaper, followed by ultrasonic cleaning in isopropanol (40 kHz, 15 min), nitrogen drying, and sputter-coating with a 5–10 nm gold layer (20 mA, 60–120 s). SEM imaging parameters included an accelerating voltage of 5–10 kV, working distance of 8–10 mm, high-vacuum mode (<5 × 10^{-4} Pa), and a secondary electron detector. Five random fields of view were captured at ×500 (50 μm) and ×200 (100 μm) magnifications, with auto-focusing and manual optimization of brightness (30%–50%) and contrast (20%–40%). The ×500 images were quantitatively analyzed in Fiji to determine pore and particle size distributions, while the ×200 images assessed macroscopic homogeneity. Representative images were labeled as " ×500, 50 μm" and " ×200, 100 μm" (as illustrated in Fig. 1).

2.2. Preparation of epoxy-impregnated MgO matrix

MgO matrices compacted at five pressures (30, 40, 50, 60, and 70 MPa) were prepared as described in Section 2 and stored in a desiccator. During molding, moistened MgO powder was filled into a polished stainless-steel mold (inner diameter 30.05 mm). After pre-pressing at 5 MPa to fix the powder, a 12-mm-diameter hemispherical copper electrode was embedded using tweezers, and the inter-electrode distance was precisely adjusted to 2.40 ± 0.05 mm using calipers before applying the target pressure. After post-drying and cooling, an M3-threaded brass column was screwed into the electrode to ensure mechanical stability at the electrode–copper column interface during impregnation (Aouadja et al., 2022). The epoxy resin system comprised E51 epoxy resin and polyetheramine curing agent (4:1 vol ratio), mixed at 100 rpm for 2 min until transparent and homogeneous, followed by degassing in a vacuum oven (40 kPa, 10 min). Concurrently, the inner wall of the combined steel mold and copper sheets (0.5 mm thick) on matrix sides was spray-coated with a 5–10 μm fluorocarbon release agent and baked at 150 °C for 40 min to form an anti-adhesion layer. During impregnation, the MgO/hemispherical electrode assembly was fixed in the mold, and degassed resin was injected under constant pressure until the matrix top surface was fully covered (1.0 ± 0.2 mm). Vacuum (40 kPa) was maintained for 10 min to drive resin infiltration via capillary action and negative pressure synergistically. Curing proceeded at 50 °C for 4 h. After cooling to room temperature, demolding and copper sheet removal yielded MgO/EP composite matrices with electrode spacing deviation < ±2% and defect-free interfaces (as shown in Fig. 2; matrix shown in Fig. 3). Subsequently, ~2 mm specimens were taken from each MgO/EP matrices adjacent to the two hemispherical electrodes and scanned by micro-CT using an Xradia 620 Versa (ZEISS, Germany) to examine the epoxy resin's infiltration distribution and pore filling within the matrix.

2.3. Choice of electrode geometry and material

Hemispherical electrodes were selected because their smooth curvature produces a controlled, reproducible field distribution: curvature gives a predictable degree of field concentration without the singularities of sharp edges, which facilitates direct

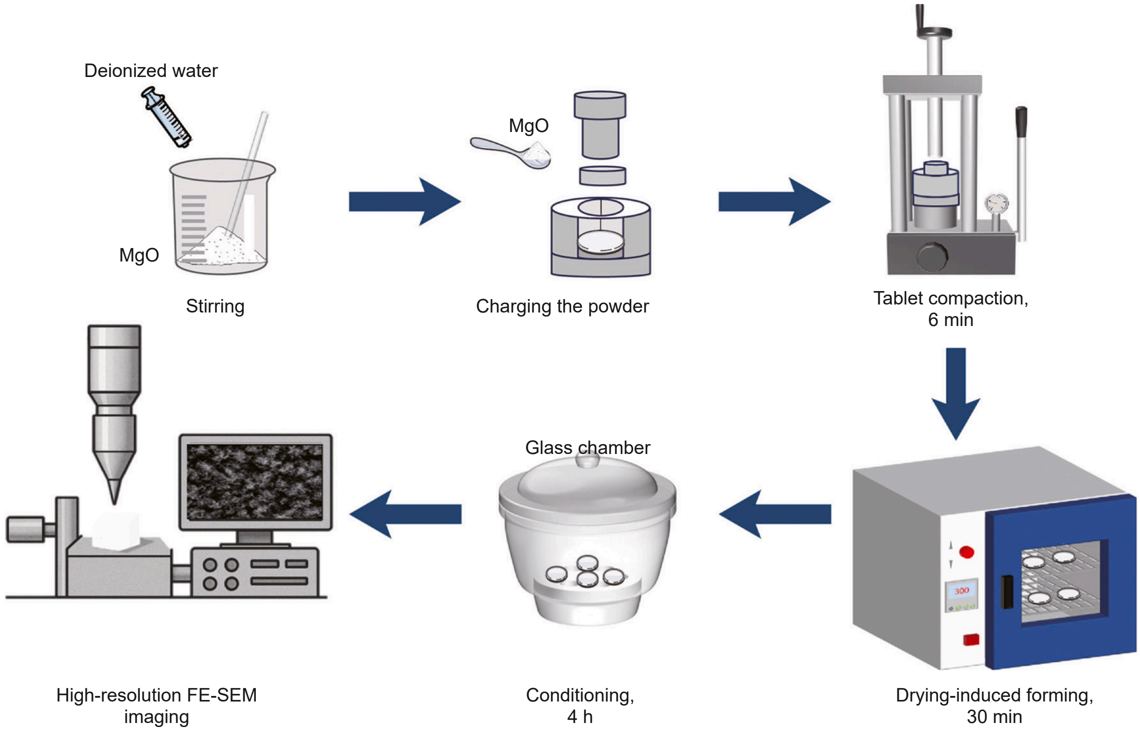

Fig. 1. Flowchart of MgO pellet preparation and observation.

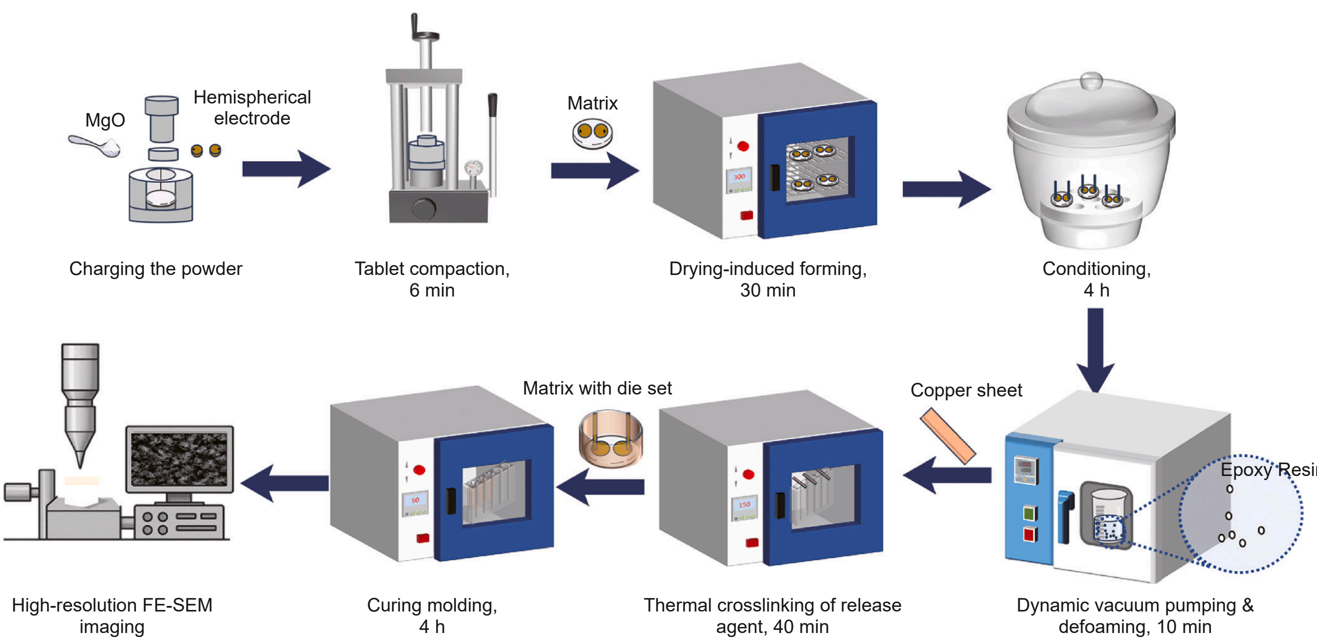

Fig. 2. Flowchart of MgO/EP matrix preparation and observation.

comparison between experiment and electrostatic simulation and between surface-flashover and bulk-puncture modes. Where applicable we followed the procedural elements of ASTM D149 (ASTM International, 2020) and IEC 60243-1 (International Electrotechnical Commission, 2013) (electrode cleaning/conditioning, precise gap control, and defined voltage-ramp and breakdown detection criteria) so that our measurements are reproducible and comparable with standard dielectric tests; the hemispherical geometry also maps naturally onto the surface-test configurations used in these standards while remaining well suited to CT-informed pore-scale modeling.

Copper was chosen as the electrode material for practical and application-driven reasons. The heater and power cable conductors in the target device are copper, so copper electrodes reproduce the actual conductor–insulator interface and allow consistent electrostatic boundary conditions between lab tests and device-scale simulations. Copper's high conductivity, ease of machining and stable polished finish improve test repeatability and minimise

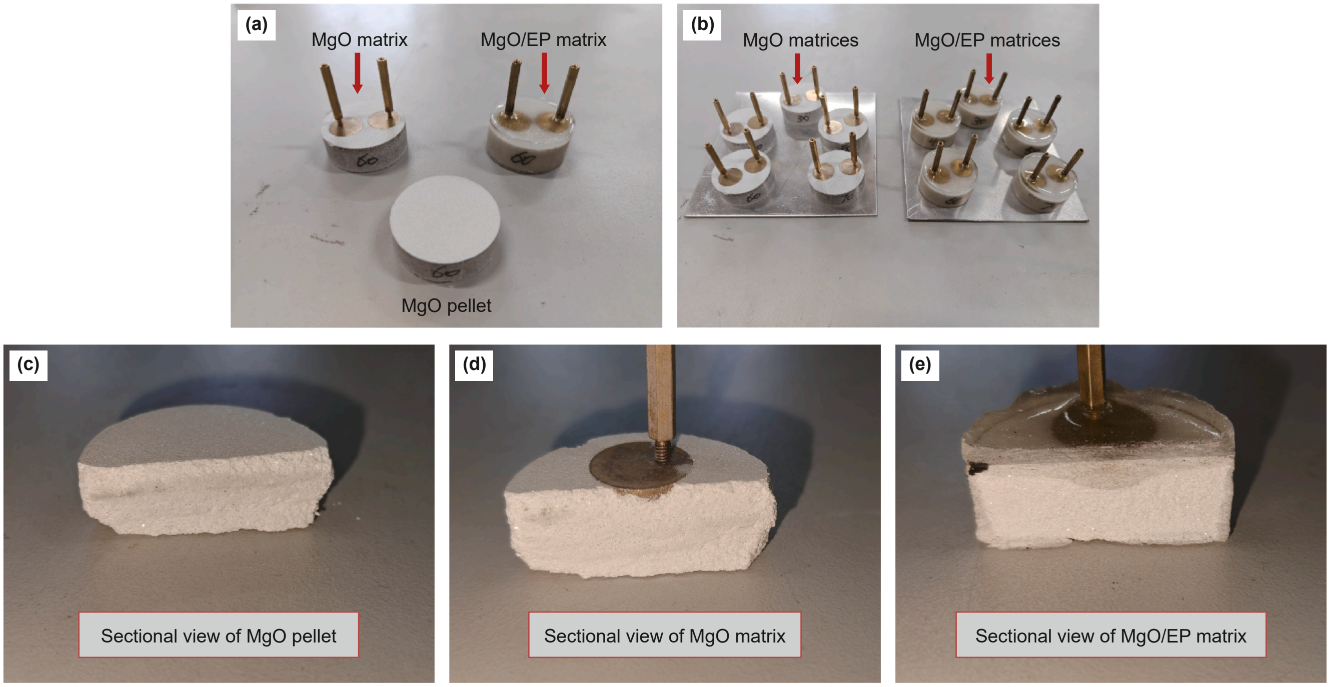

Fig. 3. Representative photograph and sectional view of the actual sample. (**a**) MgO pellet, MgO matrix and MgO/EP test matrix. (**b**) Matrices from the same batch tested at 30–70 MPa. (**c**) Sectional view of MgO pellet. (**d**) Sectional view of MgO matrix. (**e**) Sectional view of MgO/EP matrix.

contact-resistance artefacts, consistent with the metallic-electrode recommendations implicit in ASTM D149 (ASTM International, 2020) and IEC 60243-1 (International Electrotechnical Commission, 2013).

2.4. Dielectric strength testing of MgO matrices

Before testing, both non-impregnated and EP-impregnated MgO matrices were removed from the desiccator and equilibrated at 26 °C and constant humidity for 2 h. Electrodes were connected via the pre-embedded method: a copper alligator clip linked the positive terminal of a high-voltage DC source (HDGT10 kV, Huading Power) to the top of the copper column. The negative terminal was connected to the base of the copper column in non-impregnated MgO matrices with a 1.00 ± 0.05 mm air gap, and directly to the cured layer surface and copper column base in MgO/EP composites. The grounding end was connected to an independent ground stud via a shielded cable (impedance <0.1 Ω) to form a closed circuit (Geng et al., 2018). Matrixes were fixed on a wooden, insulated platform to prevent movement. Voltage was ramped continuously at 0.1 kV/s using a portable withstand voltage tester (HDGT10 kV) with real-time current monitoring. Breakdown was identified upon the current surge to 1 mA with an audible alarm, and the breakdown voltage was recorded. Each matrix type was tested three times, and average breakdown voltages were calculated to compare dielectric strength before and after EP impregnation (test setup shown in Fig. 4).

3. Multiphysics numerical model

3.1. Pore structure modeling of MgO matrix

To address the limitations of internal sensor embedment and sparse measurement points in testing, a one-way coupled multiphysics model of two-phase flow (phase-field), creeping flow, and electrostatics was developed in COMSOL Multiphysics. First, the phase-field method was used to simulate epoxy resin infiltration into the MgO porous matrix, and the resulting dielectric distribution was fed into the electrostatics module to compute the electric field strength. Pore structure parameters were derived from SEM images and Fiji analysis (Zhao et al., 2005), with experimental data sourced from laboratory measurements and calibrated against prior studies (Das et al., 2022; Djoudi et al., 2015; White et al., 2015). For each pressing pressure (30, 40, 50, 60, and 70 MPa), SEM cross-sectional images at ×500 magnification (50-μm scale bar) were acquired. Grayscale images were imported into Fiji, where the Weka Segmentation plugin (Arganda-Carreras et al., 2017) labeled MgO skeletons and pore matrices to train a random forest classifier for generating binary images. Equivalent pore channel width and particle diameter were then quantified via “Analyze Particles”.

Based on pore width and particle diameter parameters at each pressure level, 2D representative elements of rounded polygonal skeletons and tunnel-like pore channels were reconstructed in CAD. These geometries were imported into COMSOL for meshing and combined simulations, ensuring microstructural differences in experiments were accurately reflected. Pearson correlation coefficients between experimental and simulated pore/particle sizes were calculated in Origin for all pressures, constructing a 5 × 5 correlation matrix. The correlation plot plugin generated a heatmap where color intensity (blue: R→1, red: R→ −1) visualized correlation strength.

3.2. Epoxy-air phase infiltration model using phase field method

3.2.1. Fluid model establishment

The two-phase flow phase field method was coupled with the creeping flow interface in COMSOL Multiphysics to simulate epoxy/air infiltration in the MgO matrix (Fei et al., 2023; Jafari et al., 2021; Zhou et al., 2019). The fluid was modeled as incompressible flow with negligible inertial terms (i.e., omitting convection terms in Stokes flow), retaining only viscous and Darcy

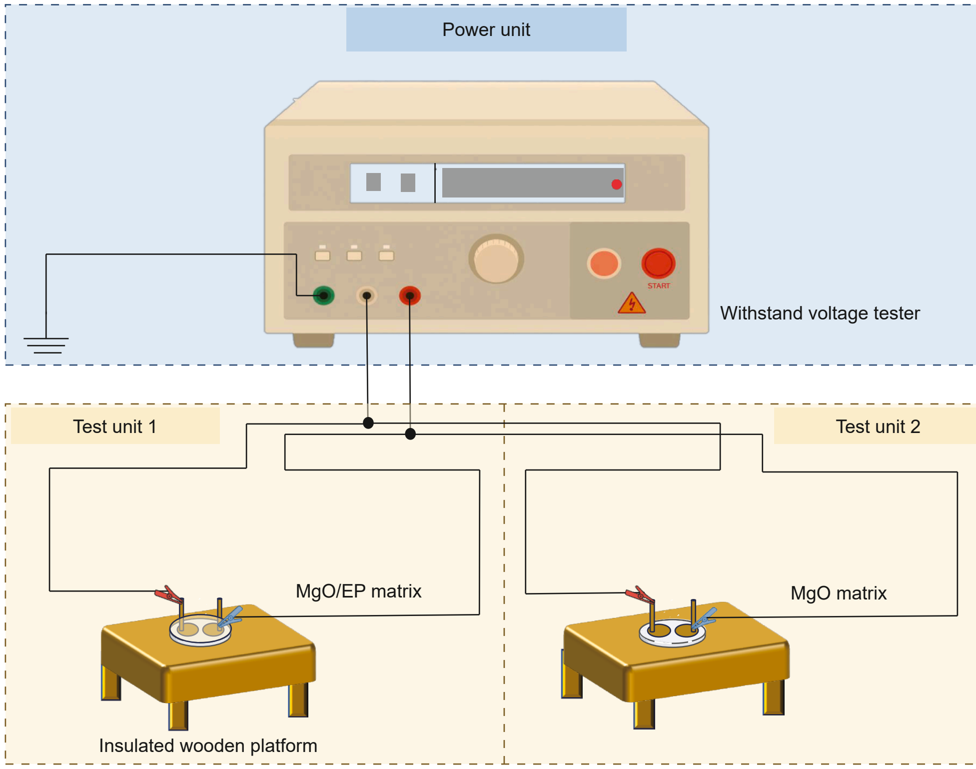

Fig. 4. Breakdown voltage test setup for MgO and MgO/EP matrices.

resistance terms. The core of the model comprises four principal components: peristaltic flow hydrodynamics, phase-field evolution, the two-phase flow coupling framework, and a non-Newtonian constitutive model for the epoxy resin.

(1) Peristaltic flow hydrodynamics

$$\rho\frac{\partial \boldsymbol{u}}{\partial t} = \nabla\cdot\left[-p\boldsymbol{I} + \mu\left[\nabla\boldsymbol{u} + (\nabla\boldsymbol{u})^{\mathrm{T}}\right]\right] + \boldsymbol{F}_{\mathrm{st}} + \rho g$$

$$\nabla\cdot\boldsymbol{u} = 0$$

$\boldsymbol{u}$ is the fluid penetration velocity; ρ is the mixture density, interpolated between air (ρ_{air}) and epoxy (ρ_{EP}) via the phase field. Flow is driven by the pressure gradient ∇p and viscous stress, with viscosity μ given by a volume-fraction-weighted average. The body force is dominated by the capillary force $\boldsymbol{F}_{\mathrm{st}}$ from surface tension at the pore walls (driving resin penetration). At the same time, gravity (ρg) is included for completeness but is negligible at the microscale.

(2) Phase-field evolution

$$\frac{\partial\phi}{\partial t} + \boldsymbol{u}\cdot\nabla\phi = \nabla\cdot\left(\frac{\gamma\lambda}{\epsilon_{\mathrm{pf}}^2}\nabla\psi\right)$$

$$\psi = -\nabla\cdot\left(\epsilon_{\mathrm{pf}}^2\nabla\phi\right) + \left(\phi^2 - 1\right)\phi + \frac{\epsilon_{\mathrm{pf}}^2}{\lambda}\frac{\partial f}{\partial\phi}$$

ϕ is the phase-field variable ($\phi = +1$ for epoxy, -1 for air). The convective term $\boldsymbol{u}\cdot\nabla\phi$ advects the resin front, while diffusion and chemical-potential terms smooth the interface and dissipate interfacial energy. ϵ_{pf} sets the interface thickness, λ (related to surface tension σ) defines interfacial energy, γ controls evolution rate, and $f(\phi)$ is the free-energy density.

(3) Two-phase flow coupling

In the simulation, to ensure a smooth transition of material properties between air and resin, we introduce a Heaviside function $H(\cdot)$ to interpolate the density continuously:

$$\rho = \rho_{\mathrm{air}} + (\rho_{\mathrm{EP}} - \rho_{\mathrm{air}})H\left(\frac{\phi+1}{2}\right)$$

When $\phi \to +1$ (EP), $\rho \to \rho_{\mathrm{EP}}$; when $\phi \to -1$ (air), $\rho \to \rho_{\mathrm{air}}$. Likewise, the mixture viscosity is

$$\mu = \mu_{\mathrm{air}}\frac{1-\phi}{2} + \mu_{\mathrm{EP}}\frac{1+\phi}{2}$$

where μ_{air} is the air viscosity and μ_{EP} is given by the non-Newtonian constitutive model. The capillary body force is written as

$$\boldsymbol{F}_{\mathrm{st}} = \left(\frac{\lambda}{\epsilon_{\mathrm{pf}}^2}\psi - \frac{\partial f}{\partial\phi}\right)\nabla\phi$$

Which is the key driver of phase separation and epoxy infiltration.

(4) Non-Newtonian constitutive model

The epoxy's shear-thinning in micro-pores is described by the Carreau-Yasuda model:

$$\mu_{\mathrm{EP}} = \mu_\infty + (\mu_0 - \mu_\infty)\left[1 + (\lambda\dot{\gamma})^a\right]^{\frac{n-1}{a}}, \dot{\gamma} = \sqrt{2\boldsymbol{S}:\boldsymbol{S}}$$

where $\dot{\gamma}$ is the local shear rate, μ_0 and μ_∞ are the zero- and infinite-shear viscosities, λ is the relaxation time, $\boldsymbol{S}$ is the strain rate tensor, n and a govern thinning intensity and transition sharpness. This formulation ensures high viscosity at low shear and rapid viscosity

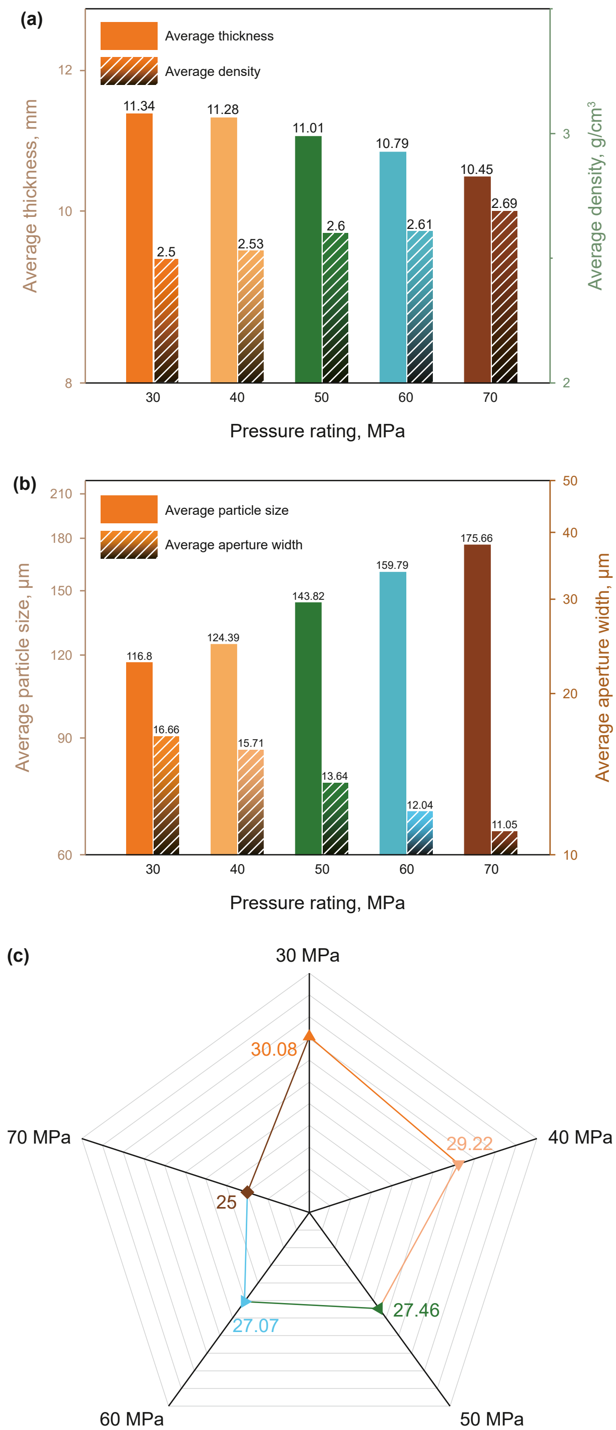

Fig. 5. Physical properties of MgO matrices. (**a**) Average thickness h and density ρ. (**b**) Average particle size and pore width. (**c**) Average porosity.

drop under high shear, matching observed resin penetration behavior.

3.2.2. Boundary conditions

For the two-phase flow-phase-field, creeping flow simulation, the inlet pressure P_0 follows a time-dependent trend:

$$P_0 = 6000 \cdot step1(t) \cdot \exp(-t\,/\,tau)(\mathrm{Pa})$$

where, $step1(t)$ is a smoothed step function (eliminating pressure jumps for numerical stability), and the exponential term $\exp(-t\,/tau)$ characterizes EP injection pressure attenuation characteristics, tau is the time constant of characteristic attenuation. The outlet boundary is defined as $P_0 = 0$ Pa, with "suppress backflow" enabled. The solid-fluid interface was applied with no-slip condition ($u = 0$) and phase field flux constraint ($n \cdot \nabla\phi = 0$) to prevent fluid penetration into the porous skeleton.

Initial conditions: porous channels were fully air-filled ($\phi = -1$), the EP injection zone was defined as $\phi = 1$. Wall wettability was implemented via contact angle boundary conditions (Syakur et al., 2017): the contact angle between inner walls of the pore channels and EP was set as $\theta_w = \pi/6$ rad, and $\theta_w = \Pi/2$ rad for outer walls to replicate observed EP retention. Surface tension coefficient was set to 0.03 N/m. Material properties: EP was defined by the Carreau-Yasuda model (no elastic shear thinning), with zero-shear-rate viscosity $\mu_0 = 35$ Pa·s and infinite-shear-rate viscosity $\mu_\infty = 7$ Pa·s were measured using a Borealis DV2T viscometer, relaxation time $\lambda = 0.1$ s (Zare et al., 2019), flow index $n = 0.4$ (Khechiba et al., 2017), transition parameter $a = 1.5$ (Nazir et al., 2021). Air was defined as Newtonian fluid (dynamic viscosity $\mu_{air} = 1.81 \times 10^{-5}$ Pa·s). Contact angle data was measured using a Kino SL250 Optical Contact Angle Meter & Interface Tensometer.

3.3. Finite-element electrostatic field model and combining strategy

3.3.1. Establishment of electrostatic field model

The EP filling distribution from phase field simulations was mapped to the electrostatics module. Equivalent dielectric constant was calculated via phase field variable ϕ:

$$\varepsilon_r(\varphi) = \varepsilon_{air}\frac{1-\phi}{2} + \varepsilon_{epoxy}\frac{\phi+1}{2}$$

where, $\varepsilon_{air} = 1$, $\varepsilon_{epoxy} = 4.5$, the relative dielectric constants of MgO and the copper electrode were set as $\varepsilon_{MgO} = 9$ and $\varepsilon_{Cu} = 1$, respectively. The electrostatic-field governing equation based on the same porous medium grid was obtained as:

$$\nabla \cdot [\varepsilon_0 \varepsilon_r(\phi)\nabla V] = 0, E = -\nabla V$$

where, vacuum dielectric constant $\varepsilon_0 = 8.854 \times 10^{-6}$ nF·mm^{-1}, V and E represent electric potential (V) and electric field intensity (V/mm), respectively. The step iteration workflow was:

(1) Solve infiltration-phase field equation at each phase-field time step to update $\phi(x, y, t)$.
(2) Update global $\varepsilon_r(\phi)$ based on $\phi(x, y, t)$.
(3) Solve steady-state electrostatic field equation.

Steady-state iterations continued until phase-field convergence, systematically revealing post-filling electric-field distortion and providing quantitative insights for optimizing the dielectric properties of heater-end-sealing materials.

3.3.2. Boundary conditions

In the electrostatic field module, the boundary conditions are: the left hemisphere electrode surface was subjected to the experimentally measured breakdown voltage V_{bd}, while the right hemisphere electrode surface, as well as the left, right, and bottom walls, were set as grounded ($V = 0$), and the remaining outer walls were treated with an insulating boundary condition ($n \cdot \varepsilon_r \nabla V = 0$).

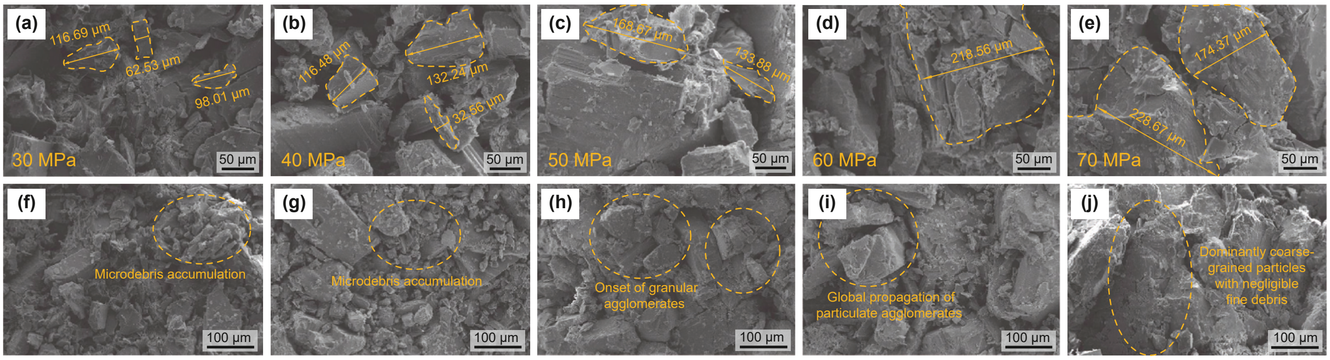

Fig. 6. Microstructure of MgO matrices under 30–70 MPa pressing pressure at ×200 and ×500 scales. (**a**–**e**) Particle morphology under 30–70 MPa (×200). (**f**–**j**) Overall microstructure under 30–70 MPa (×500).

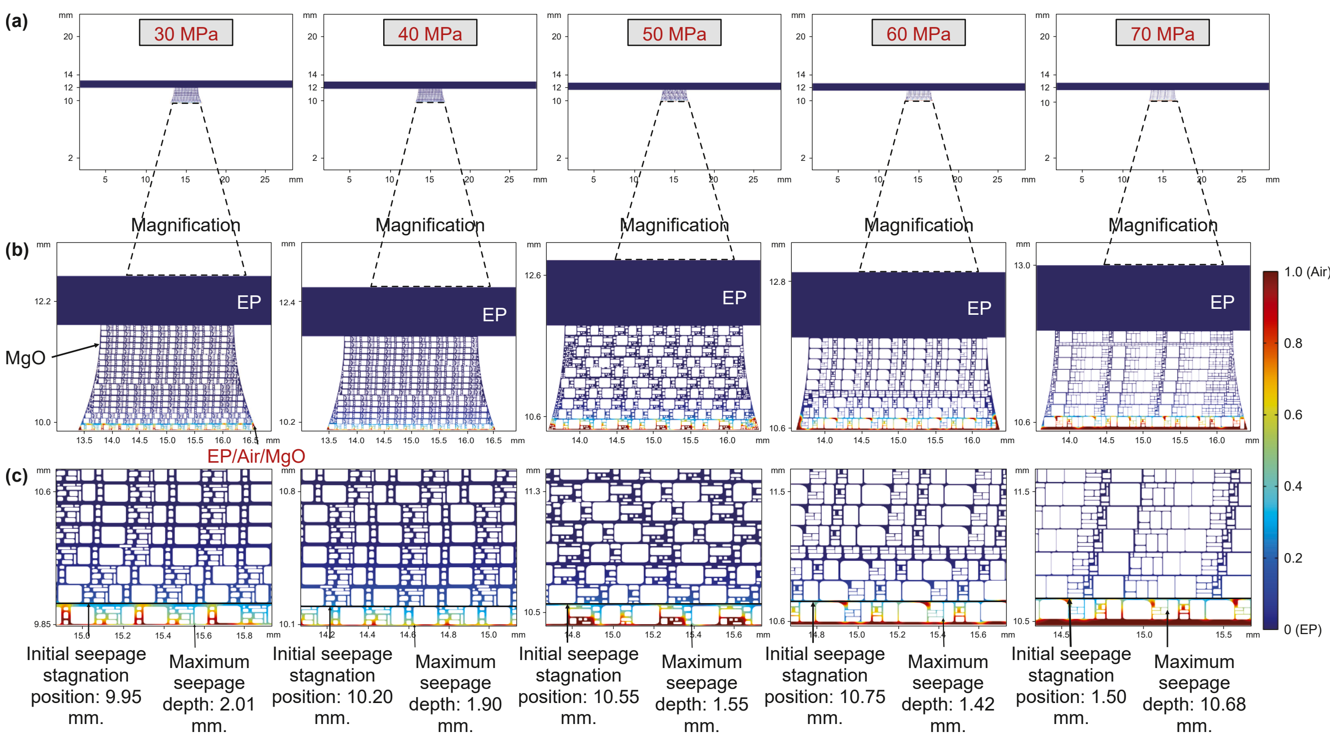

Fig. 7. Global simulated infiltration patterns under varying pressures. (**a**) Global simulation. (**b**) Local simulation. (**c**) Local simulation and infiltration depth.

To accurately characterize the charge distribution, the material domain is defined as follows:

1. Solid charge conservation domain: hemispherical electrode and MgO skeleton regions, the dielectric constant was set as $\varepsilon_{Cu} = 1$ for Cu, and $\varepsilon_{MgO} = 9.7$ for MgO.
2. Fluid charge conservation domain: pore channels and epoxy-filled regions, the dielectric constant was assigned by component proportion: $\varepsilon_{air} = 1$ for air and $\varepsilon_{epoxy} = 4.5$ for EP.

This configuration enabled one-way coupled electric field calculations across solid-liquid-gas phases via interface potential continuity ($[[V]] = 0$) and spatial distribution function $\varepsilon_r(\varphi)$ of dielectric constants, effectively capturing the electric-field enhancement at the interface induced by discontinuities in dielectric permittivity.

4. Results and analysis

4.1. Influence mechanism of pressure on the densification behavior of MgO matrixes

Analysis of pressed and dried MgO matrices (fixed diameter $R_D = 30.05 \pm 0.1$ mm) revealed the regulatory mechanism of pressure on the densification behavior of the material. Bar plots (Fig. 5(a)) showed that density ρ increased nonlinearly with pressing pressure, rising from 30 MPa ($\rho = 2.50$ g/mm^3) to 70 MPa ($\rho = 2.69$ g/mm^3), while matrix thickness decreased from 11.34 (30 MPa) to 10.45 mm (70 MPa). As illustrated in Fig. 5(a–c), pore width decreased progressively with increasing pressure, whereas particle size increased and porosity declined.

FE-SEM analysis (Fig. 6(a–j)) highlighted significant microstructural differences under various pressures:

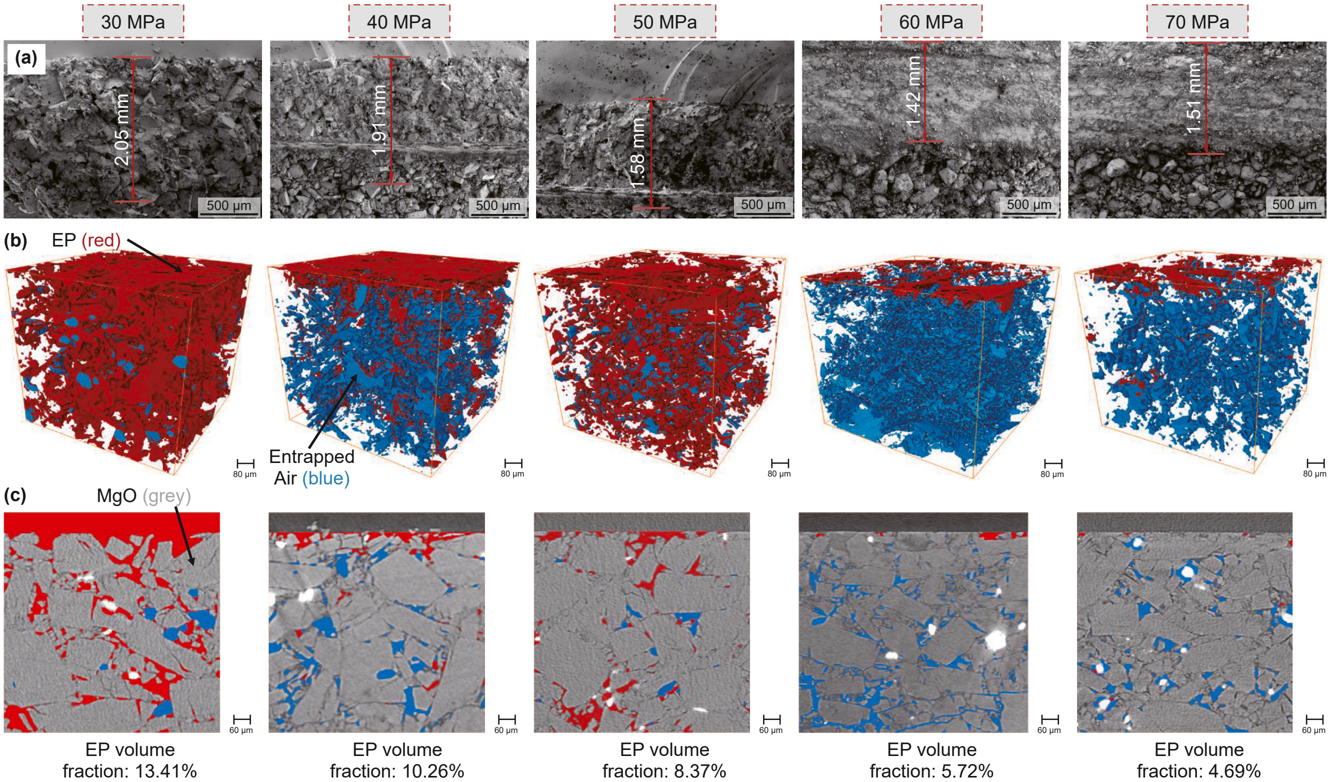

Fig. 8. EP penetration distance within the MgO matrix under different compaction pressures, along with the corresponding 3D CT skeleton model and cross-sectional views of the penetrated regions. (**a**) Plot of penetration distance versus compaction pressure. (**b**) 3D-CT skeleton models of the penetrated EP regions under different compaction pressures. (**c**) Cross-sectional views of the 3D-CT skeleton models.

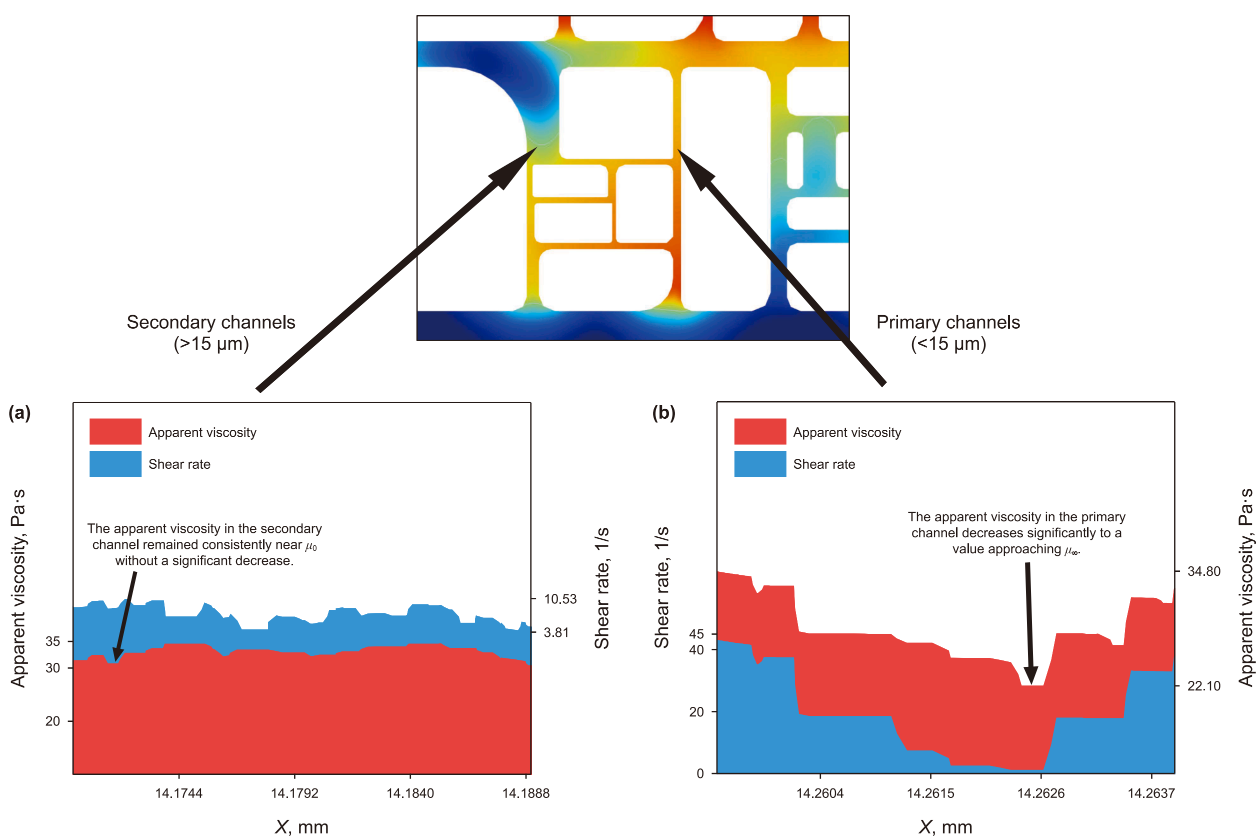

Fig. 9. Shear rate and apparent viscosity in the primary and secondary channels under a pressing pressure of 60 MPa. (**a**) Shear rate and apparent viscosity in the secondary channels. (**b**) Shear rate and apparent viscosity in the primary channels.

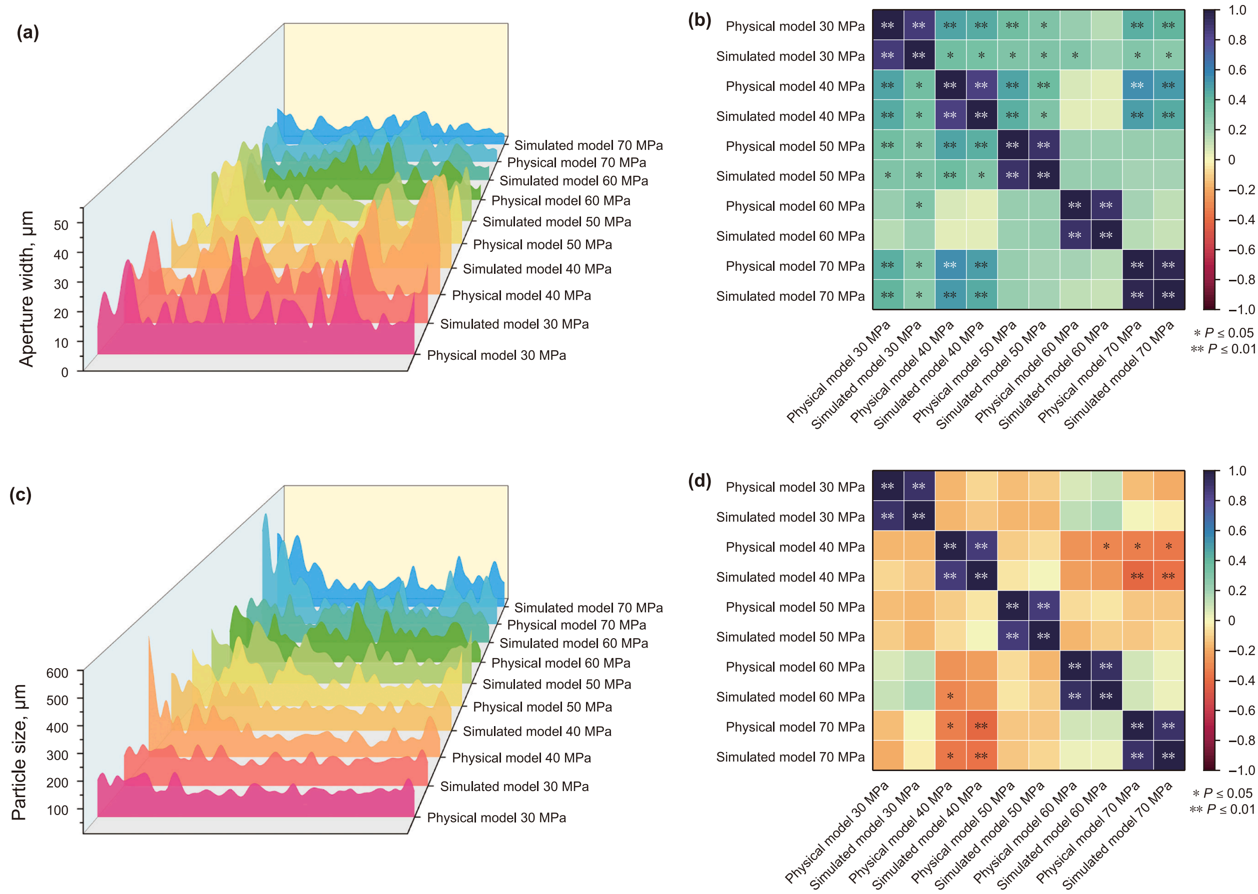

Fig. 10. Physical vs. simulated pore width/particle size trends and correlation heatmaps. (**a**) Pore width trend comparison. (**b**) Pore width correlation. (**c**) Particle size trend comparison. (**d**) Particle size correlation.

Low-pressure matrixes (30–40 MPa): dominated by loose debris particles (30–40 μm) and open pores, with porosity of 30.08%–29.22%.

Medium-pressure matrices (40–50 MPa): reduced porosity (27.46%) due to particle rearrangement; small clusters of particle aggregates (>60 μm) observed at 50 MPa.

High-pressure matrices (60–70 MPa): continuous particle aggregates (>100 μm), with porosity drastically reduced to 27.07%–25.00%.

The drying protocol (gradient heating to 300 °C) further enhanced pore closing efficiency and structural stability. FE-SEM images (Fig. 6(a–j)) confirmed that high-pressure matrices (60–70 MPa) exhibited strengthened interparticle mechanical interlocking at interfaces under synergistic pressure-heating effects, significantly reducing pore width and increasing uniform particle aggregate size. In contrast, low-pressure matrices (30–40 MPa) retained open pores (porosity 30.08%–29.22%) due to their high initial connectivity, resulting in only localized shrinkage via liquid-phase evaporation. These results demonstrate that pressing pressure regulates pore networks (open → closed transition) through particle dynamics (sliding → particle rearrangement → interparticle mechanical interlocking), while the drying process drives interface bonding via thermally activated diffusion.

4.2. Regulatory mechanism of pore structure on the infiltration path of EP

Results indicate that in the low-pressure range (30–40 MPa), larger pore widths (15.79–16.66 μm, Fig. 7(b) and (c)) enabled infiltration depths of 1.91–2.05 mm (Fig. 8(a)), which is aligned with simulation results of 1.90–2.01 mm (as shown in Fig. 7(a–c), in which blue = EP phase, red = air phase, white = MgO). EP infiltrated smoothly along multiple parallel channels with flat interfaces (Fig. 7(b)). In the medium-pressure range (50–60 MPa), reduced pore widths (12.04–13.64 μm, Fig. 7(c)) limited infiltration depth to 1.42–1.58 mm (simulation error <5%), with local stagnation and interface undulations at secondary channels at the front end of infiltration (Fig. 7(b) and (c)). At high pressure (70 MPa), the average pore width decreased further to 11.05 μm, resulting in a sharp decline in infiltration depth (1.51 mm; simulation: 1.50 mm). EP flowed primarily through primary (smaller) channels (<15 μm) at the front end of infiltration. In comparison, minimal infiltration occurred in secondary (larger) channels (>15 μm), leading to significant air entrapment at branches (See Figs. 7(c) and 9).

By performing image analysis on the 3D CT reconstructions obtained from samples compacted at different pressures, the volume fraction of EP within the MgO matrix (EP proportion) was quantified. The results show a monotonic decrease in resin proportion as compaction pressure increases from 30 to 70 MPa: 13.41% at 30 MPa, 10.26% at 40 MPa, 8.37% at 50 MPa, 5.72% at 60 MPa, and 4.69% at 70 MPa (See Fig. 8(b)). Notably, although the penetration depth at 70 MPa partially recovered relative to 60 MPa (rising from approximately 1.42 to 1.51 mm), the resin proportion at 70 MPa (4.69%) remained the lowest across all pressure conditions. The cross-sectional views indicate that under this high-pressure condition the resin preferentially formed fast penetration paths along a small number of principal channels, while the

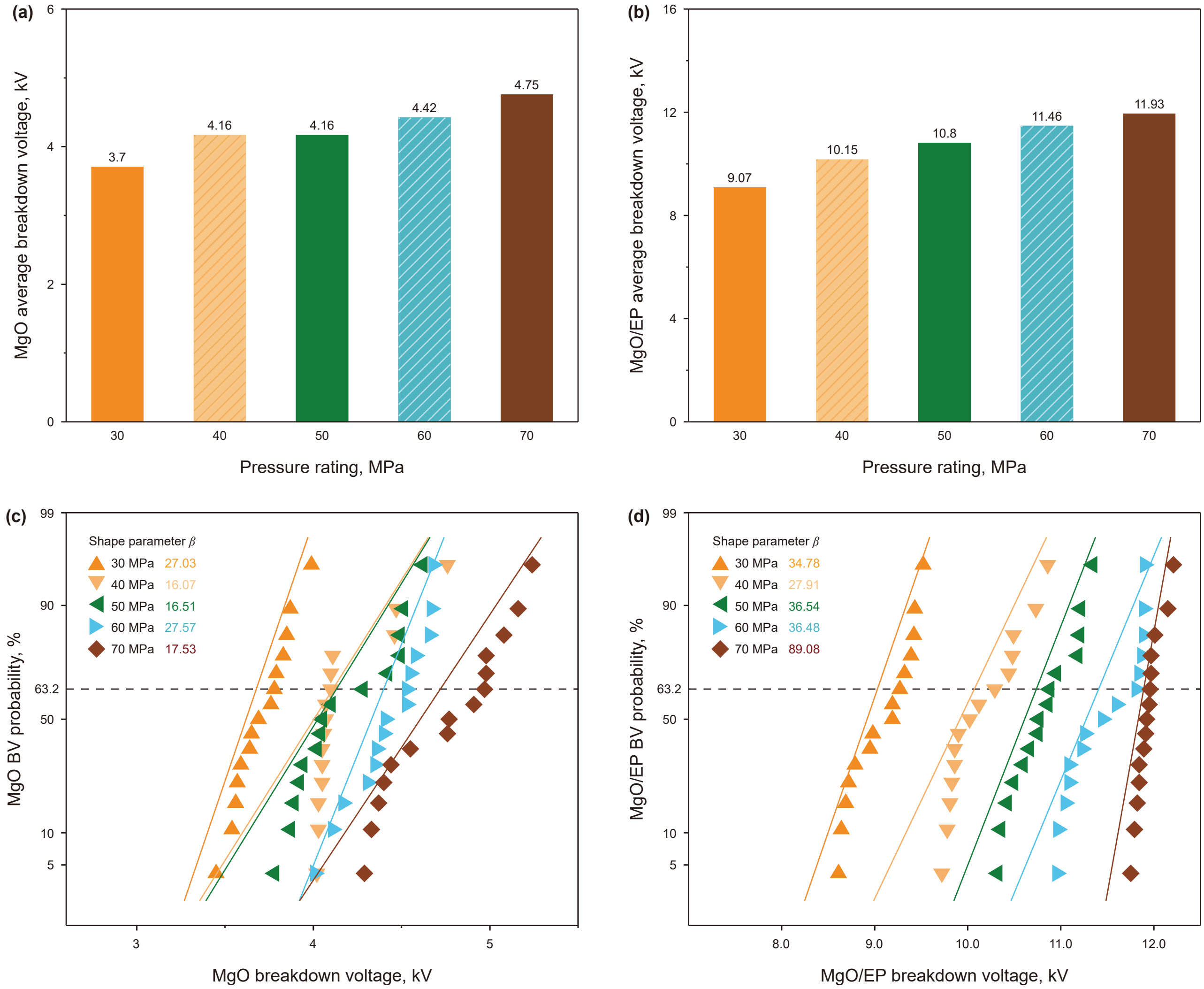

Fig. 11. Average breakdown voltages and Weibull distributions for MgO and MgO/EP matrices. (**a**, **b**) Average breakdown voltages. (**c**, **d**) Weibull distributions of breakdown probability.

majority of secondary channels were not effectively filled (Fig. 8(c)).

Mechanistic analysis indicates that the apparent viscosity of the epoxy $\mu(\dot{\gamma})$ approximates its zero-shear value μ_0 when the shear rate $\dot{\gamma} \ll 1/\lambda$. As the $\dot{\gamma}$ increases significantly, the Carreau-Yasuda model,

$\mu_{EP} = \mu_\infty + (\mu_0 - \mu_\infty)[1 + (\lambda\dot{\gamma})^a]^{\frac{n-1}{a}}$ predicts shear-thinning behavior with $\mu(\dot{\gamma}) \to \mu_\infty$ (shear stress $\tau = \mu(\dot{\gamma})\dot{\gamma}$, and $\dot{\gamma} \sim \boldsymbol{u}/R$). A reduction in pore radius R elevates $\dot{\gamma}$ and reduces $\mu(\dot{\gamma})$ (See Fig. 9), so local velocity $\boldsymbol{u}$ must increase to maintain a constant injection rate, thereby enhancing shear thinning and lowering μ (Datta et al., 2014). However, permeability scales as $K \propto R^2$ and thus drops sharply, causing Darcy resistance to rise proportionally (Tosco et al., 2013). Consequently, in the 30–50 MPa range, $\dot{\gamma}$ remains below $1/\lambda$ so that μ does not decrease markedly, the modest Darcy resistance together with stable capillary forces permits resin infiltration through both primary and secondary channels. At 60–70 MPa, $\dot{\gamma}$ exceeds the λ^{-1} threshold, μ rapidly approaches μ_∞, and the primary channel—experiencing lower shear viscosity—supports higher flow rates. In contrast, the secondary channel, with larger R and much greater Darcy resistance, is impeded (Fig. 9).

4.3. Validation of simulation-experiment correlation

Experimental observations and numerical simulations showed high consistency in microstructural parameters. As shown in Figs. 10(a) and 5(b), the pore width of both the actual matrixes and the simulation models decreased significantly as the pressing pressure dropped from 30 to 70 MPa, the actual values decreased from 16.66 to 11.05 μm, while the simulated values decreased simultaneously from 17.01 to 10.41 μm, with the maximum relative error being less than 6%; the particle size analysis also showed the same trend (Figs. 10(c) and 5(b)): the average particle size increased from 116.8 to 175.66 μm, and the simulation value increased from 120.66 to 171.88 μm. To quantitatively evaluate the structural fitting degree (Hutchinson and Grimm, 2022), this study constructed a 5 × 5 Pearson correlation matrix and presented it in a heatmap (Fig. 10(b) and (d)): the correlation coefficients for each pore width dimension under different pressure conditions were all >0.85

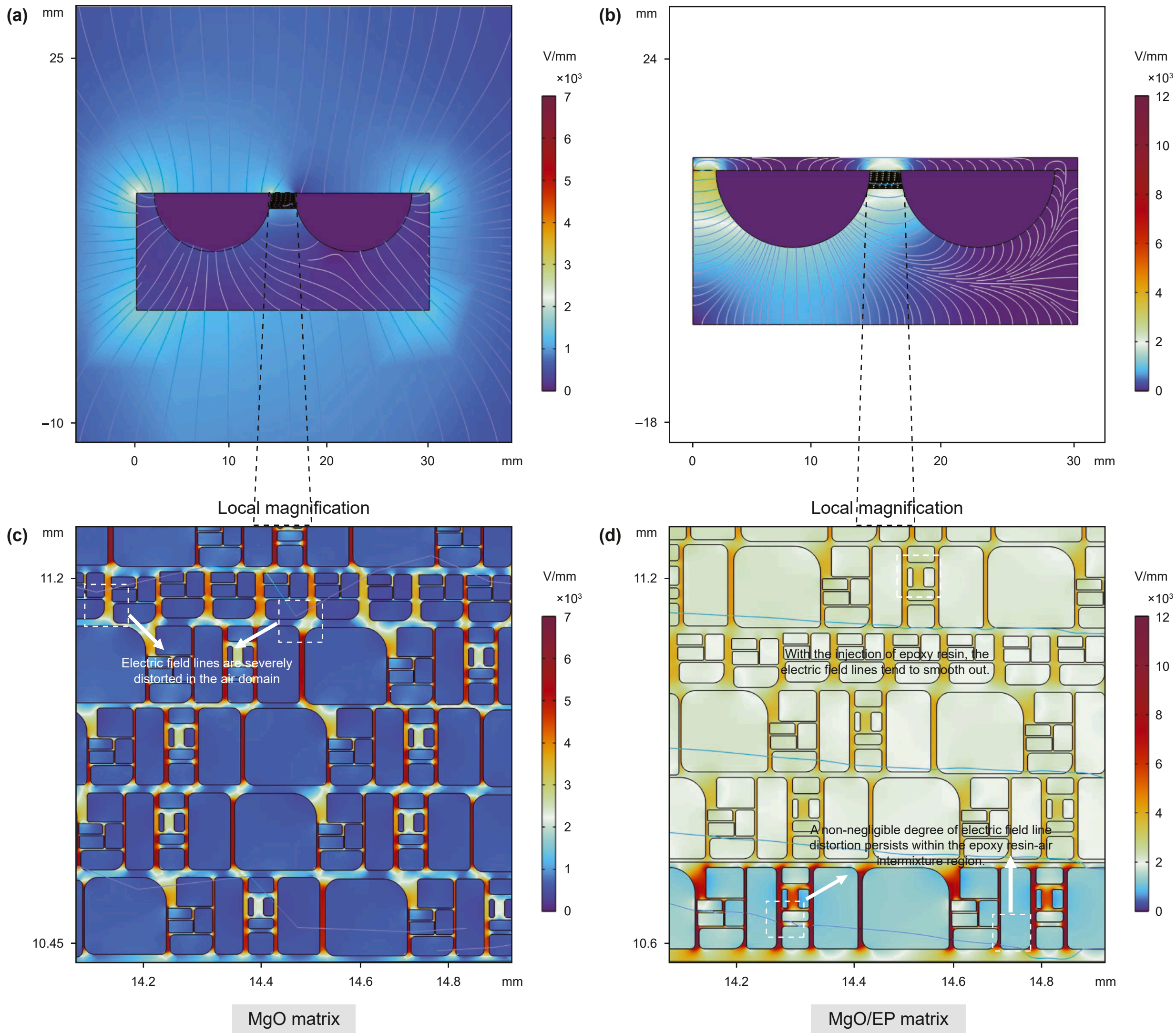

Fig. 12. Global field strength and local electric field lines and field strength distribution diagrams of MgO and MgO/EP matrices under different pressing pressures. (**a**, **b**) Global field strength distribution. (**c**, **d**) Local field strength and electric field line distribution.

(P < 0.05), indicating that the simulation model can faithfully reconstruct the pore structure under different compaction conditions; the particle size also maintained a high correlation in the medium-pressure range (>0.85, P < 0.05), but decreased to 0.10 in the 30 MPa/70 MPa ranges, reflecting the structural differences under extreme compaction conditions that exceed the fitting ability across intervals. Overall, the above results verified that the two-dimensional structural model constructed from FE-SEM images and machine learning segmentation exhibits excellent consistency and adaptability, providing a reliable geometric basis for subsequent combined simulation of infiltration and the electric field.

4.4. Breakdown characteristics of MgO/EP vs. MgO catrices

Breakdown voltages of non-impregnated MgO and epoxy-filled MgO/EP matrices were statistically analyzed using a-two-parameter Weibull distribution. Fig. 11(a) and (c) present the bar chart and Weibull probability graph of the breakdown voltages of non-impregnated MgO matrixes under different pressing pressures (30, 40, 50, 60, and 70 MPa), the corresponding characteristic breakdown voltages are 3.70, 4.16, 4.16, 4.42, and 4.75 kV, showing a clear trend of increasing with the increase in pressure. In contrast, Fig. 11(b) and (d) show that the characteristic breakdown voltages of MgO/EP matrices rose from 9.07 to 11.93 kV, representing a 2.3-fold overall enhancement over non-impregnated matrices owing to the effective resin filling; within the 60–70 MPa range, this increase plateaus. Moreover, the epoxy resin infiltration not only markedly enhances the breakdown strength (increased $\alpha = 63.2\%$) but also homogenizes the internal structure by eliminating pores and interfacial defects, thereby yielding more uniform breakdown initiation and improving the reliability of the dielectric breakdown performance. The Weibull shape parameter β exceeded 10 for both matrix types, indicating highly concentrated, low-dispersion breakdown voltage distributions; notably, β values for MgO/EP matrixes were significantly higher than those for MgO matrixes, confirming the enhanced distribution uniformity achieved through epoxy filling.

4.5. EP infiltration and local electric field distortion

First, electrostatic field simulations were conducted on pure MgO matrices under 30–70 MPa to calculate the global and local electric field strengths and field-line distributions along the radial and axial directions of the pores, as shown in Fig. 12(a) and (c). Subsequently, under identical boundary conditions, the local infiltration depths obtained from phase-field simulations were

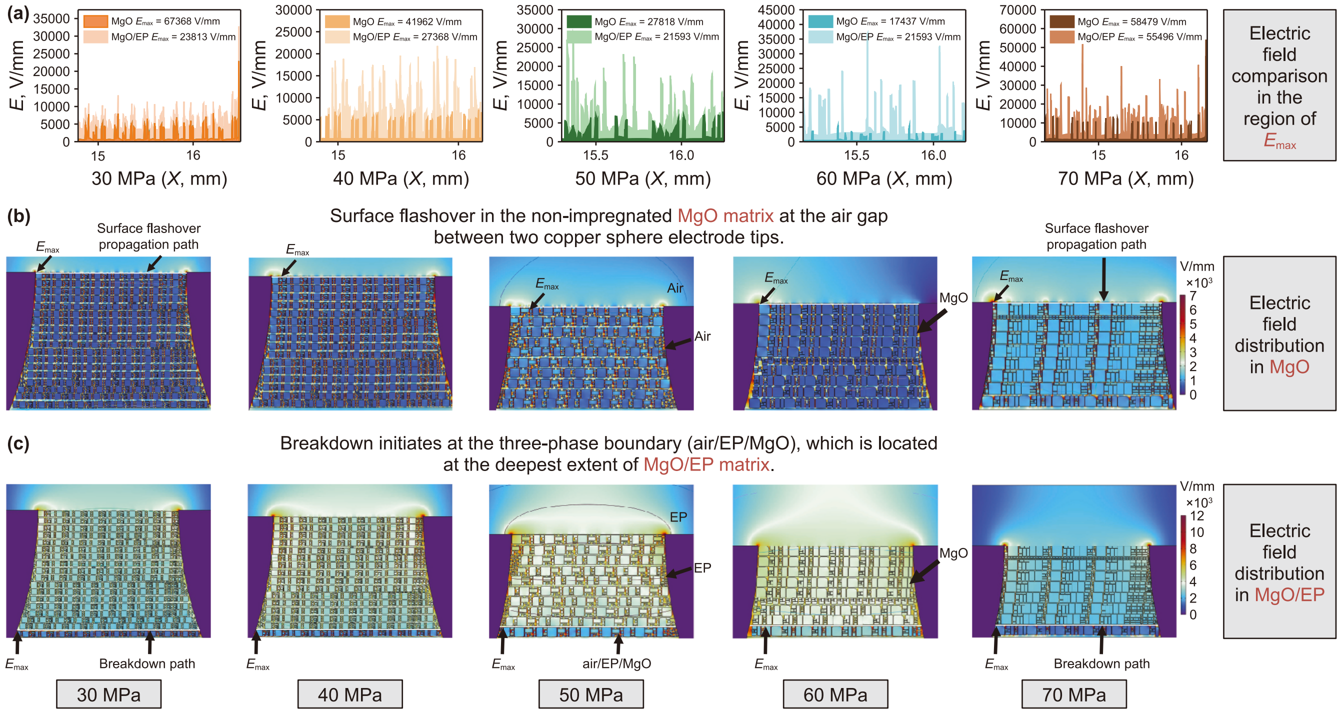

Fig. 13. Comparison of the local maximum field strength and the electric field strength near the maximum field strength under different pressing pressures for MgO and MgO/EP matrices. (**a**) Comparison of the maximum field strength. (**b**) Local electric field strength of MgO matrices. (**c**) Local electric field strength of MgO/EP matrices.

mapped to assign dielectric constants. The electrostatic field was re-simulated for the MgO/EP composite system, as illustrated in Fig. 12(b) and (d). The results reveal that before EP injection, high electric fields were concentrated in the air and pores above the hemispherical anode. After EP injection, the high-field regions shifted to the matrix edges near the anode and the inter-electrode pores. Moreover, EP injection significantly reduced the peak local electric field: for the 30 MPa matrices (Fig. 13), the maximum electric field strength decreased from 67,368 to 23,813 V/mm (a reduction of ≈65%), while for the 40 MPa matrices, it dropped from 41,962 to 27,368 V/mm (a reduction of ≈35%). These findings conclusively demonstrate that EP injection effectively mitigates electric field distortion caused by MgO pores and air.

Analysis of the electric field strength results for MgO and MgO/EP matrices (Fig. 12(c) and (d) and Fig. 13(b) and (c)) shows that before EP infiltration, the abrupt change in dielectric constants between the MgO skeleton ($\varepsilon_{\mathrm{EP}} = 9$) and air ($\varepsilon_{\mathrm{air}} = 1$), coupled with the sharp geometric morphology of the pores, caused electric field lines to “escape” and concentrate at the pore wall edges, creating localized high-field regions. After EP infiltration, the replacement of air with EP ($\varepsilon_{\mathrm{EP}} = 4.5$) reduced the dielectric ratio from 9:1 to 9:4.5, resulting in a more uniform electric field distribution. Simultaneously, the geometric smoothing effect of EP on pore boundaries further weakened the field concentration at sharp positions. The increased dielectric constant in the filled regions allowed more electric field lines to pass through originally low-field regions. The overall field strength expanded into the higher-middle value range, leading to optimized global and local maximum field strengths, consistent with the electric field distribution near the maximum, as depicted in Fig. 13(a).

The electrostatic simulations further elucidate the experimentally observed shift in breakdown location following epoxy impregnation. In the unfilled configuration, the peak electric field is concentrated in surface air gaps between the electrodes, consistent with the measured surface flashover. When a wetting front is present, however, the simulated field maps show a pronounced relocation of the local field maximum toward the termination of the impregnating front. This relocation arises from the permittivity discontinuity and the geometric edge formed at the EP/MgO/air three-phase contact field, which together produce a local field intensification sufficient to trigger breakdown at lower applied voltages than those required within the fully impregnated bulk (breakdown propagation path (white reference line) in Fig. 13(b) and (c)). The simulations, therefore, rationalize the observed correlation between impregnation depth and breakdown initiation site (Fig. 13(b) and (c)) and imply that partial filling—despite increasing bulk permittivity—can create new, locally vulnerable regions at the wetting front (See Fig. 7(c)).

5. Conclusions

Based on systematic experiments and multiphysics simulations of the MgO/EP composite system under five pressing pressures (30–70 MPa), the following key conclusions are drawn:

(1) Influence of pressing pressure on the densification behavior of MgO matrix

The synergistic effects of dry pressing and high-temperature drying resulted in a nonlinear increase in the apparent density of the matrices with increasing pressing pressure, accompanied by a significant reduction in pore width. The particle aggregation transitioned from loose fragments to continuous clusters, forming a more closed and uniform pore network at high pressure (60–70 MPa). These results validate the mechanism by which pressing pressure regulates pore structure through sliding, particle rearrangement, and interparticle mechanical interlocking.

(2) Infiltration mechanism of EP in the pore network

Consistent with phase-field creeping-flow simulations and experimental observations, CT image analysis shows a monotonic decline in epoxy volume fraction with increasing compaction pressure (13.41% → 10.26% → 8.37% → 5.72% → 4.69% from 30 to 70 MPa), reflecting the progressive reduction of accessible pores and flow pathways. At low pressures (30–50 MPa), larger pores and lower Darcy resistance facilitate uniform infiltration through multiple channels. At high pressures (60–70 MPa), shear-thinning lowers the apparent viscosity in primary channels, improving their infiltration while secondary channels begin to close, which increases gas entrapment and contributes to the observed decline in epoxy volume fraction.

(3) Enhancement of dielectric breakdown performance by EP filling

Weibull statistical analysis shows that the breakdown voltage of unfilled MgO matrices increased from 3.70 to 4.75 kV with rising pressing pressure. Under the same conditions, MgO/EP matrices exhibited breakdown voltages ranging from 9.07 to 11.93 kV, surpassing unfilled matrices by approximately 5.4–7.2 kV. Additionally, the Weibull shape parameter β for both matrix types exceeded 10, with higher β values observed in EP-filled matrices, indicating a more concentrated breakdown-voltage distribution and improved material reliability.

(4) Mitigation mechanism of local electric field distortion after EP filling

Electrostatic simulations and experiments show that epoxy infiltration substantially reduces electric-field distortion at MgO pore/air interfaces. Before infiltration, high-field regions concentrate in air-filled pores above the electrodes, leading to surface-initiated breakdown. After infiltration, these regions shift toward electrode edges and primary pore channels, and the peak field strength drops markedly—from 67,368 and 41,962 V/mm (30 and 40 MPa) to 23,813 V/mm (65% reduction) and 27,368 V/mm (35% reduction). This improvement results from dielectric constant matching and geometric smoothing, which suppress local field concentration and improve field uniformity. As a result, breakdown in unfilled specimens originates at surface air gaps, whereas in partially impregnated specimens it relocates to the EP/MgO/air three-phase wetting front.

In summary, this study systematically reveals the evolution of pore structures in MgO/EP composites from open networks to closed uniformity under pressing pressure, as well as the mechanism by which EP filling mitigates local electric field distortion and improves breakdown voltage. These findings provide a valuable reference for the design of end-sealing materials in high-power downhole electric heaters.

CRediT authorship contribution statement

Hong-Liang Zhang: Writing – original draft, Funding acquisition, Methodology, Software, Supervision, Validation. **Shu-Xuan Li:** Methodology, Validation, Visualization, Writing – original draft, Writing – review & editing. **Si-Liang Du:** Investigation, Methodology, Project administration. **Ying-Xin Zhang:** Data curation, Formal analysis. **Su-Fang Li:** Resources, Software. **Hai Jin:** Project administration, Supervision. **Yao-Min Liu:** Formal analysis, Funding acquisition. **Tao Wu:** Resources, Supervision.

Declaration of competing interest

The authors declare that they have no known competing financial interests or personal relationships that could have appeared to influence the work reported in this paper.

Acknowledgement

This work was supported by the Key Core Technology Research Project of China National Petroleum Corporation (No. 2024ZG23), 2026 Gansu Education Department “Innovation Star” Program (No. 2026CXZX-584) and National Natural Science Foundation of China (No. 52367017).

References

Agrawal, A, Satapathy, A, 2014. Thermal and dielectric behavior of epoxy composites filled with ceramic micro particulates. J. Composit. Mater. 48 (30), 3755–3769. https://doi.org/10.1177/0021998313513205.

Akin, F., Arikan, O., 2022. Analysis of breakdown mechanism based on contact area and field enhancement factor of different electrode-material combinations. Int. J. Energy Res. 46 (9), 12674–12686. https://doi.org/10.1002/er.8036.

Aliyu, B.D., Rohani, M.N.K.H., Musa, U., et al., 2024. Simulation of partial discharge phenomenon in epoxy-resins insulation under very low and high stressing frequencies. In: Proceedings of the 2024 IEEE International Conference on Power Engineering Application (ICPEA). https://doi.org/10.1109/ICPEA60617.2024.10499042.

Aouadja, F., Bouzerara, F., Guvenc, C.M., et al., 2022. Fabrication and properties of novel porous ceramic membrane supports from the diatomite and alumina mixtures. Bol. Soc. Espanola Ceram. Vidr. 61 (5), 531–540. https://doi.org/10.1016/j.bsecv.2021.04.002.

Arganda-Carreras, I., Kaynig, V., Rueden, C., et al., 2017. Trainable weka segmentation: A machine learning tool for microscopy pixel classification. Bioinformatics 33 (15), 2424–2426. https://doi.org/10.1093/bioinformatics/btx180.

ASTM International, 2020. Standard Test Method for Dielectric Breakdown Voltage and Dielectric Strength of Solid Electrical Insulating Materials at Commercial Power Frequencies. ASTM International, West Conshohocken, PA. ASTM D149-20.

Cao, M., Li, L., Guo, R.Z., et al., 2023. Excellent dielectric properties and finite element simulation of Al–epoxy composites with constructed ultrathin Al_2O_3 parallel-plate microcapacitors. ACS Appl. Mater. Interfaces 15 (26), 31595–31607. https://doi.org/10.1021/acsami.3c01391.

Castillo, S.M., Muñoz, S., Trueba, P., et al., 2019. Influence of the compaction pressure and sintering temperature on the mechanical properties of porous titanium for biomedical applications. Metals 9 (12), 1249. https://doi.org/10.3390/met9121249.

Cha, H.A., Ha, S.J., Jo, M.G., et al., 2024. Three-dimensional MgO filler networking composites with significantly enhanced thermal conductivity. Adv. Compos. Hybrid Mater. 7 (5), 178. https://doi.org/10.1007/s42114-024-01004-3.

Chen, Y., Zeng, H., Wang, J., et al., 2022. Heat transfer performance of a downhole electric tubular resistive heater. Appl. Sci. 12 (19), 9508. https://doi.org/10.3390/app12199508.

Das, P., Sarifuddin, N., Rana, J., et al., 2022. Unsteady solute dispersion in the presence of reversible and irreversible reactions. Proc. R. Soc. A 478 (2264), 20220127. https://doi.org/10.1098/rspa.2022.0127.

Datta, S.S., Ramakrishnan, T.S., Weitz, D.A., 2014. Mobilization of a trapped non-wetting fluid from a three-dimensional porous medium. Phys. Fluids 26 (2), 022002. https://doi.org/10.1063/1.4866641.

Djoudi, H., Gelin, J.C., Barrière, T., 2015. Experiments and FE simulation for twin screw mixing of nanocomposite of polypropylene/multi-walled carbon nanotubes. Compos. Sci. Technol. 107, 169–176. https://doi.org/10.1016/j.compscitech.2014.12.017.

Fei, F., Costa, A., Dolbow, J.E., et al., 2023. A phase-field model for hydraulic fracture nucleation and propagation in porous media. arXiv preprint arXiv:2304.13197. https://doi.org/10.48550/arXiv.2304.13197.

Ge, G., Tang, Y., Li, Y., et al., 2020. Effect of environmental temperature on the insulating performance of epoxy/MgO nanocomposites. Appl. Sci. 10 (20), 7018. https://doi.org/10.3390/app10207018.

Geng, L.D., Jin, Y.M., Tan, D.Q., et al., 2018. Computational study of nonlinear dielectric composites with field-induced antiferroelectric–ferroelectric phase transition. J. Appl. Phys. 124 (16), 164109. https://doi.org/10.1063/1.5051725.

Ha, S., Moon, Y.K., Choi, J., et al., 2025. Simple protein foaming-derived 3D segregated MgO networks in epoxy composites with outstanding thermal conductivity properties. Adv. Sci., e06465 https://doi.org/10.1002/advs.202506465.

Hassan, A., Yutkin, M., Chandra, V., et al., 2021. Quality evaluation of epoxy pore casts using silicon micromodels: Application to confocal imaging of carbonate samples. Appl. Sci. 11 (12), 5557. https://doi.org/10.3390/app11125557.

Hutchinson, L.G., Grimm, O., 2022. Integrating digital pathology and mathematical modelling to predict spatial biomarker dynamics in cancer immunotherapy. NPJ Digital Medicine 5 (1), 92. https://doi.org/10.1038/s41746-022-00636-3.

International Electrotechnical Commission (IEC), 2013. IEC 60243-1: Electrical insulation—Test methods—Part 1: Tests at Power Frequencies. Geneva: IEC.

Jafari, A., Vahab, M., Broumand, P., et al., 2021. An eXtended finite element method implementation in COMSOL multiphysics: thermo-hydro-mechanical modeling of fluid flow in discontinuous porous media. arXiv preprint arXiv:2112.11918. https://doi.org/10.48550/arXiv.2112.11918.

Kang, Z., Zhao, Y., Yang, D., 2020. Review of oil shale in-situ conversion technology. Appl. Energy 269, 115121. https://doi.org/10.1016/j.apenergy.2020.115121.

Karlis, A., 2021. Investigation of factors affecting partial discharges on epoxy resin: simulation, experiments, and reference on electrical machines. Energies 14 (20), 6621. https://doi.org/10.3390/en14206621.

Khechiba, K., Mamou, M., Hachemi, M., et al., 2017. Effect of Carreau-Yasuda rheological parameters on subcritical Lapwood convection in horizontal porous cavity saturated by shear-thinning fluid. Phys. Fluids 29 (6), 063101. https://doi.org/10.1063/1.4986794.

Kurimoto, M., Kato, T., Yoshida, T., et al., 2019. Low permittivity epoxy nanoporous composites filled with hollow nanosilica. IET Nanodielect. 2 (3), 109–113. https://doi.org/10.1049/iet-nde.2018.0040.

Liu, H.Q., Jun, Y., Deng, Y.M., 2015. Study of the properties of non-gas dielectric capacitors in porous media. Pet. Sci. 12 (1), 104–113. https://doi.org/10.1007/s12182-015-0015-z.

Melnikov, G.M., Belov, E.P., Panyaev, V.M., et al., 1970. Testing of a downhole electric heater with hydraulic sealing of the cable housing. Neftepromysl. Delo (6), 19–21.

Nazir, U., Sohail, M., Selim, M.M., et al., 2021. Finite element simulations of hybrid nano-Carreau–Yasuda fluid with Hall and ion slip forces over rotating heated porous cone. Sci. Rep. 11 (1), 19604. https://doi.org/10.1038/s41598-021-99116-z.

Rodríguez-Serna, J.M., Albarracín-Sánchez, R., Dong, M., et al., 2020. Computer simulation of partial discharges in voids inside epoxy resins using three-capacitance and analytical models. Polymers 12 (1), 77. https://doi.org/10.3390/polym12010077.

Shui, H., Wang, Y., Liu, Z., et al., 2023. Optimal parameter adjustment of catalytic combustion heaters for oil shale in-situ conversion of low calorific value gases. J. Clean. Prod. 426, 139020. https://doi.org/10.1016/j.jclepro.2023.139020.

Syakur, A., Hermawan, Sutanto, H., 2017. Determination of hydrophobic contact angle of epoxy resin compound silicon rubber and silica. IOP Conf. Ser. Mater. Sci. Eng. 190 (1), 012025. https://doi.org/10.1088/1757-899X/190/1/012025.

Tosco, T., Marchisio, D.L., Lince, F., et al., 2013. Extension of the Darcy-Forchheimer law for shear-thinning fluids and validation via pore-scale flow simulations. Transport Porous Media 96 (1), 1–20. https://doi.org/10.1007/s11242-012-0070-5.

White, K.L., Hawkins, S., Miyamoto, M., et al., 2015. Effects of aspect ratio and concentration on rheology of epoxy suspensions containing model plate-like nanoparticles. Phys. Fluids 27 (12), 123306. https://doi.org/10.1063/1.4937145.

Xia, H., Settles, N., Dewire, D., 2019. Moisture-resistant sealing materials for downhole HPHT electrical feedthrough package. J. Microelect. Electron. Pack. 16 (3), 141–148. https://doi.org/10.4071/imaps.942864.

Yatimi, Y., Mendil, J., Marafi, M., et al., 2024. Advancement in heavy oil upgrading and sustainable exploration emerging technologies. Arab. J. Chem. 17 (3), 105610. https://doi.org/10.1016/j.arabjc.2024.105610.

Yu, S., Chen, Z., Xiao, H., et al., 2025. Research on heat conduction and performance optimization of electric heating ultra-high performance concrete pavement snow melting and ice removal systems in cold regions. Therm. Sci. Eng. Prog. 65, 103987. https://doi.org/10.1016/j.tsep.2025.103987.

Zare, Y., Park, S.P., Rhee, K.Y., 2019. Analysis of complex viscosity and shear thinning behavior in poly(lactic acid)/poly(ethylene oxide)/carbon nanotubes biosensor based on Carreau-Yasuda model. Results Phys. 13, 102245. https://doi.org/10.1016/j.rinp.2019.102245.

Zhang, W., Yao, J., Gao, Y., et al., 2015. Analysis of electrokinetic coupling of fluid flow in porous media using a 3-D pore network. J. Petrol. Sci. Eng. 134, 150–157. https://doi.org/10.1016/j.petrol.2015.04.013.

Zhao, F., Landis, H.R., Skerlos, S.J., 2005. Modeling of porous filter permeability via image-based stochastic reconstruction of spatial porosity correlations. Environ. Sci. Technol. 39 (1), 239–247. https://doi.org/10.1021/es035228b.

Zhou, S., Zhuang, X., Rabczuk, T., 2019. Phase-field modeling of fluid-driven dynamic cracking in porous media. Comput. Methods Appl. Mech. Eng. 350, 169–198. https://doi.org/10.1016/j.cma.2019.03.001.